Effectiveness of Active Cooling on Torque Performance for Prosthestic Applications

by

Ava E. Chen

Submitted to the Department of Mechanical Engineering
in partial fulfillment of the requirements for the degree of

Bachelor of Science in Mechanical Engineering

at the

MASSACHUSETTS INSTITUTE OF TECHNOLOGY

June 2017

Signature redacted

Author .....
.....
Department of Mechanical Engineering
May 12, 2017

Signature redacted

Certified by.....
.....
Hugh M. Herr
Associate Professor
Thesis Supervisor

Signature redacted

Accepted by .....
Rohit Karnik
Professor of Mechanical Engineering, Undergraduate Officer

Effectiveness of Active Cooling on Torque Performance for Prosthestic Applications

by

Ava E. Chen

Submitted to the Department of Mechanical Engineering
on May 12, 2017, in partial fulfillment of the
requirements for the degree of
Bachelor of Science in Mechanical Engineering

Abstract

Motors used to actuate powered prostheses generally under-utilize their torque capacity due to thermal limitations of the windings. This thesis investigates the effectiveness of increasing the rate of heat transfer away from the windings in order to enable running motors at higher currents than their rated maximum levels, thus raising this torque saturation limit. Simulation models and physical prototypes based on the RCTiger 100KV U8 brushless outrunner motor were built to observe the temperature of the windings as constant current was applied to the motor. The addition of a fan-based active cooling system allowed the motor to run at 142% of its maximum continuous current rating for up to 56 seconds before winding temperatures exceeded 55°C, and limited temperature increase in simulation to 26° above ambient temperature when the full 35A stall current was applied for one second. Although the simplified circuit model was not able to fully capture nonlinear thermal behavior of the motor, simulations were able to predict approximate heating time constants and time duration before windings reached threshold temperature for current ranges 5-15A. Experimental and simulation results support the hypothesis that active cooling enables motors to run at their full torque potential for short periods of time, which holds promise for the use of cooling mechanisms in prosthetic applications.

Thesis Supervisor: Hugh M. Herr
Title: Associate Professor

Acknowledgments

Matt Carney, for suggesting this project and for providing guidance and mentorship during its course. Much of this project is the direct result of his vision and his need for meaningful answers.

Professor Hugh Herr, for being my advisor for this project and for five years of research within the Biomechatronics Lab. I am immensely grateful to have had the privilege to work directly in the field of prosthetics.

Elena Byun and **Bayley Wang**, for much-needed help tackling circuit models.
Ben Katz, for his endless encouragement and alarm-clock support.
Kris Kim, for reading too many pages.

Arthur Petron, the original mentor, for getting me excited about prostheses and mechanical engineering.

Mom, from whom all my accomplishments are derived.

Contents

List of Figures

List of Tables

Chapter 1

Introduction

A critical objective in the field of prosthetic leg design is to improve the range of dynamic movements available in a powered ankle-foot prosthesis. With current actuator technology, it is challenging to build a prosthesis matching the size and weight of the biological limb that also delivers enough instantaneous power output for explosive movements like jumping or kicking[1]. Ongoing research exists that utilize clutched and series-elastic-actuators[11] to meet torque profiles for steady-state walking gaits, but as the field moves toward using direct-drive actuators for torque controlled prostheses more consideration must be given to directly improving motor performance.

Torque provided by a motor is directly related to input current; however both winding resistance and permanent magnet flux density are dependent on temperature[8]. These effects create a saturation limit that throttles the maximum torque a motor can supply.

This thesis investigates the effectiveness of moving heat away from the critical areas of the motor in order to raise this torque saturation limit. The project approaches this challenge from both simulation and physical prototyping using the T-motor U8 brushless DC motor. Motor parameters from the U8 are used to develop simulations that predict effects of active cooling on thermal performance, which are then verified by a physical prototype. Results are then used to examine the tradeoff between added mass and package volume dedicated to manage dissipated power versus suboptimally running a larger motor in the case of a powered-ankle prosthesis.

Chapter 2

Background

2.1 Human ankle biomechanics

2.1.1 Level-ground walking

The level-ground walking gait cycle begins and ends at the heel strike of the same foot[1], and is subdivided into stance phase and swing phase. During swing phase (40% gait cycle) the foot is off the ground and the ankle does no work, but acts as a position source. Stance phase (60% gait cycle) begins when the heel strikes the ground and ends when the same foot's toe leaves the ground surface. Biokinematic studies typically separate stance phase (Figure 2-1) into three sub-phases: Controlled Plantar Flexion (CP), Controlled Dorsiflexion (CD) and Powered Plantar Flexion (PP)[3, 10]. The ankle generates the most net positive work during PP, which begins at maximum dorsiflexion and ends at toe-off. For moderate to fast walking speeds, the stored elastic energy from CD is supplemented by additional energy to generate the necessary torque for propelling the body forward. The ankle in this phase is modeled as a torque source in parallel to the CD torsion spring[1].

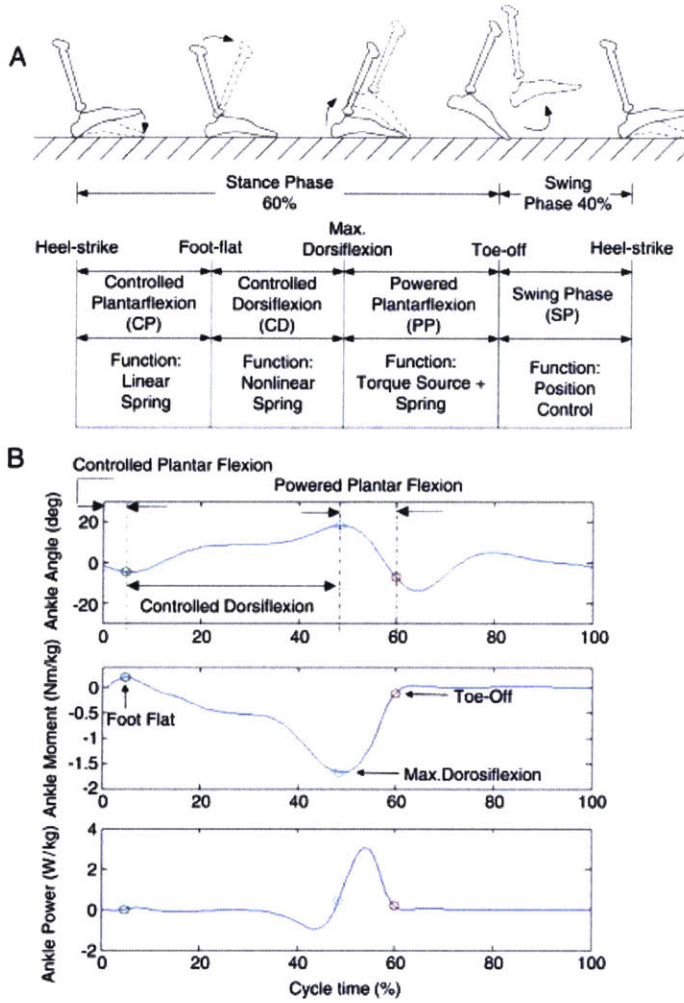

Figure 2-1: Normal human ankle biomechanics during level-ground walking. Figure taken from Au(2008). In (A), ankle behavior modeling is plotted as a function of gait phase. In (B), ankle angle, moment, and power are plotted as a function of percent of typical gait cycle. Ankle moment and power are normalized by body mass.

2.1.2 Vertical jumping

The vertical jump can also be divided into distinct stance and flight phases, where the jump cycle begins and ends with the foot flat on the ground[13]. During the flight phase (20% jump cycle), the ankle modulates position in order to optimally orient the foot, which maximizes stiffness before landing. Stance phase can be divided into pre-jump Powered Plantar Flexion (PP) and post-jump Controlled Dorsiflexion (CD) subphases. Ankle behavior is described pictorally in Figure 2-2 and in detail below.

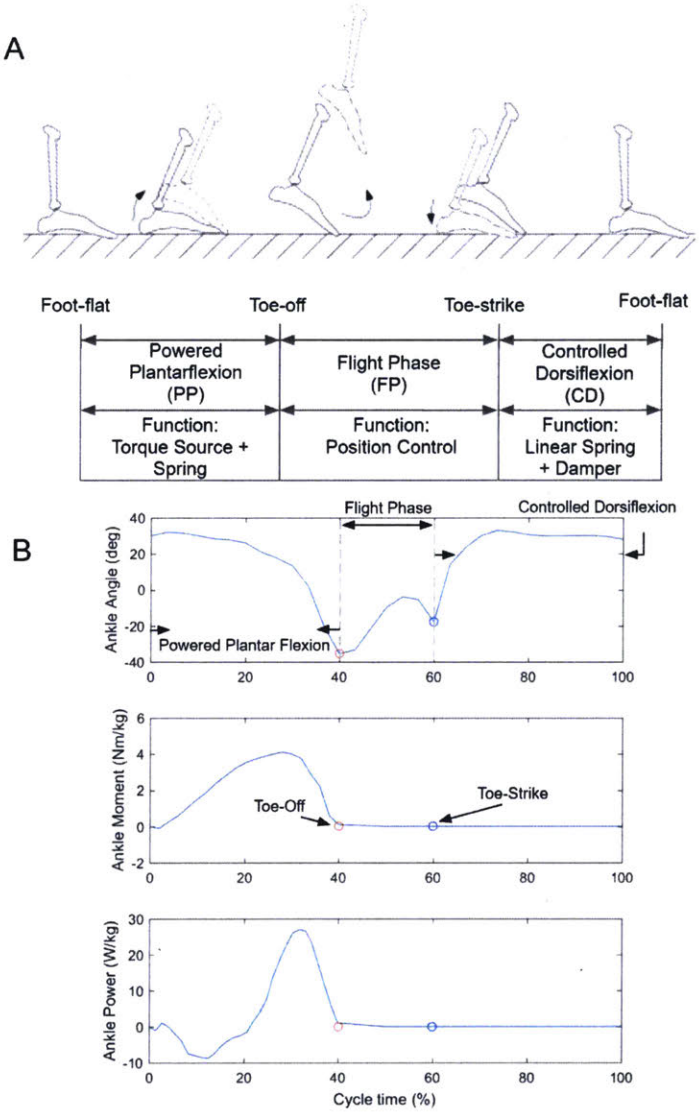

Figure 2-2: Normal human ankle biomechanics during a vertical jump. Data are from [13] and [5], replotted in the manner of [1]. In (A), ankle behavior descriptions are shown as a function of jump phase. In (B), ankle angle, moment, and power during PP are plotted as a function of percent of jump cycle (Data unavailable for JP or CD). Ankle moment and power are normalized by body mass.

Powered Plantarflexion (PP)

PP describes ankle behavior as the body propels upward, beginning from foot-flat and continuing until toe-off. The ankle supplies torque along with possible stored energy from a previous jump[13]. The ankle generates substantially more power (26.8 W/kg) than either the knee or hip joints during this phase[5].

Flight Phase (FP)

FP occurs from toe-off to toe-strike, during which the body is in the air. In the short time interval before landing, the ankle acts as a position control to reach an optimal angle and joint stiffness for toe-strike[13].

Controlled Dorsiflexion (CD)

CD begins the landing phase, starting from toe-strike until flat-foot. During this phase, the ankle decelerates the body after landing and acts as a variable damper in parallel with a linear spring[13]. With respect to joint power, the largest peak power absorptions occurs at the ankle during landing[5].

2.1.3 Torque requirements of a powered ankle-foot prosthesis

Actuators used in a prosthesis must provide sufficient stance-period work and instantaneous power output to match biological function[1]. Requirements of the prosthetic ankle include (i) varying joint stiffnesses and damping when absorbing bodyweight, (ii) modulating position during swing and flight phases, and (iii) generating large amounts of intermittent torque and net positive work for propulsion.

Current actuators have been successfully employed in stair-descent and ascent gaits[1, 4], but a powered prosthesis has not yet been able to perform a vertical jump. In order to match the biological ankle, actuators in a jumping prosthesis needs to deliver more than 3x the torque than those in previous prostheses. Additionally, such actuators would be subject to the same space and weight constraints as actuators in other powered ankle prostheses.

2.2 Torque Capacity of Electromagnetic Motors

Several actuator design parameters including gap radius and motor length, magnetic circuit, and winding material and configuration influence torque performance. These parameters determine the torque constant (K_t), voltage constant (K_v), terminal resistance (R_m), and terminal inductance (L_m) of the motor, which together describe its output torque, speed, and power[7, 8, 12]. In general use, the output torque is

assumed to be directly proportional to input current by the constant K_t.

$$\tau = K_t i \qquad \text{(in units of } \tfrac{\text{Nm}}{\text{A}}\text{)} \tag{2.1}$$

Motors are limited in torque capacity at two time scales. Instantaneous peak torque is limited by flux saturation of the magnets, beyond which additional current and accompanying greater external magentic field will not produce additional torque. The peak specific torque of a motor is defined as the following[7],

$$T_{pk} = \frac{K_t i_{sat}}{m} \qquad \text{(in units of } \tfrac{\text{Nm}}{\text{kg}}\text{)}, \tag{2.2}$$

where i_{sat} is the instantaneous current (A) resulting in magnetic flux saturation and m is the mass of the motor (kg). This peak torque capacity assumes operation that allows the motor to fully cool down between current impulses. Continuous torque capacity is limited by the thermal resistance of the windings[7],

$$T_{ts} = \frac{K_t}{m}\sqrt{\frac{1}{R_{th}R_m}} \qquad \text{(in units of } \tfrac{\text{Nm}}{\text{kg}\sqrt{^\circ\text{C}}}\text{)}, \tag{2.3}$$

where R_{th} is the thermal resistance ($\frac{^\circ C}{W}$) of the motor, R_m is electrical resistance (Ω), and m is mass (kg). Continuous torque capacity is a measure of a motor's torque production at stall compared to its waste heat dissipation[7].

Manufacturers set datasheet voltage and power ratings to ensure against thermal failure assuming that end users command voltages without monitoring winding temperature or controlling current[12]. Figure 2-3 from (Seok, 2012) describes motor performance and limits under varying operation modes.

If voltage is increased but current kept at the continuous current limit (represented by blue in Figure 2-3), motors can generate more power than suggested by the rating on the datasheet. However, applications such as human walking or jumping do not require continuous power but instead need very large torques for short periods of time. Motors can produce torques higher than the continuous operating torque limit,

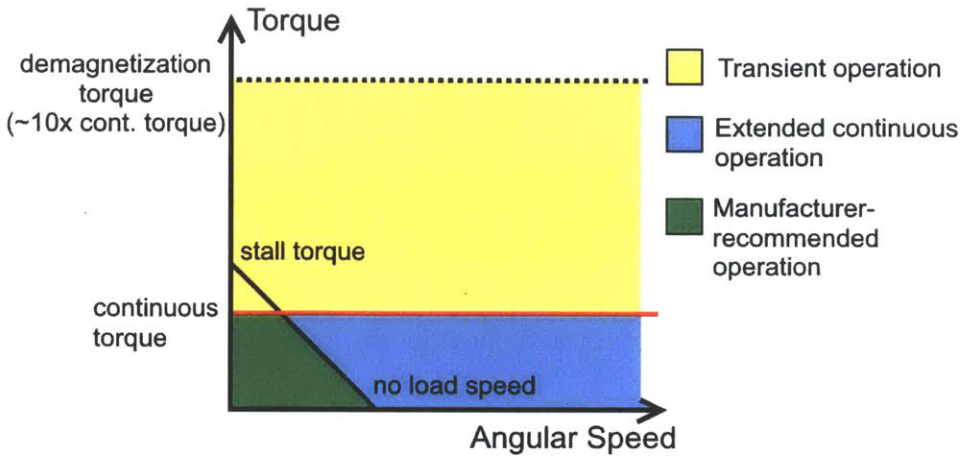

Figure 2-3: Motor performance diagram in torque-speed space under varying modes of operation taken from (Seok, 2012). Recommended operation space assumes voltage is recommended maximum.

theoretically up to the flux saturation limit of the magnets when ignoring thermal effects (represented by yellow in Figure 2-3)[12]. Operating within this transient operation space requires knowledge of the winding temperature to avoid motor thermal failure.

2.3 Effects of Elevated Temperatures on Motor Performance

The equations and metrics in the previous section assumed that the torque constant and voltage constant were, in fact, "constant." This is inaccurate. They are determined by the winding resistance and permanent magnet flux density, both of which vary as a function of temperature.

Motor winding resistance R_m is the main source of heat production within a motor. Power dissipation due to winding resistance, given by

$$P_{diss} = I^2 R_m, \tag{2.4}$$

heats up the motor. Increasing current input to the motor increases the rate of positive feedback between the rate of atomic vibrations and temperature increase within the windings. As temperature increases, electrical resistance also increases by the following equation[2, 8],

$$R_m(T) = R_{ref}\left[1 + \alpha_{conductor}\left(T - T_{ref}\right)\right], \tag{2.5}$$

where R_{ref} is the winding resistance at a reference temperature T_{ref}. For copper, the temperature coefficient $\alpha_{conductor}$ is 0.004 $(/^{\circ}C)$[8]. As temperature increases, a greater proportion of power supplied to the motor is diverted from doing useful work to being converted into waste heat that further reduces the efficiency of the motor.

Elevated temperatures in the motor also affect the permanent magnets. Increased atomic vibrations in the magnet material disturb magnetic moment alignment and cause a temporary reduction in magnetic flux density[8]. For the average NdFeB magnet, the temperature coefficient α_{magnet} is -0.0012 $(/^{\circ}C)$ and the maximum temperature T_{max} is 150 $(/^{\circ}C)$[8]. If the magnet temperature exceeds its Curie temperature, this reduction in flux density becomes permanent. The torque constant K_t is dependent on the magnetic flux density, and its dependence on temperature is given by the following equation,[2, 8]

$$K_t(T) = K_{t,ref}\left[1 + \alpha_{magnet}\left(T - T_{ref}\right)\right] \qquad \text{(in SI units)}, \tag{2.6}$$

where $K_{t,ref}$ is the torque constant at reference temperature T_{ref}. Both instantaneous torque capacity and continuous torque capacity are adversely affected by elevated motor temperatures, which effectively limit motors to suboptimal operation modes.

2.4 Convective and Conductive Heat Transfer

Excess heat produced in the motor is continuously transferred to the surrounding space via conduction, convection, and radiation. This thesis assumes negligble heat transfer by radiation and focuses instead on conductive and convective processes.

Under the two assumptions that (1) the heat transfer coefficient of the motor is independent of temperature and that (2) this coefficient is the same for the motor's surface and interior, the rate of convective cooling to the surrounding air is proportional to the temperature difference between the motor and its surroundings. The rate of heat transfer is described by Newton's law of cooling by convection[2, 6],

$$\dot{Q} = hA\big(T - T_{surr}\big), \tag{2.7}$$

in which q' is heat transferred in watts, h is the coefficient of heat transfer ($\frac{W}{m^2K}$), A is surface area (m^2), T is the motor temperature, and T_{sur} is the temperature of the surroundings. The rate of heat transfer in convection can also be expressed as a thermal resistance $R_{conv} = \frac{1}{hA}$.

The above assumptions are validated if the motor body has a sufficiently small Biot number (generally < 0.1), which indicates that (1) heat conduction within the motor is much faster than heat convection away from the surface and (2) temperature gradients are negligible within sections of the motor such that the lumped-capacitance model can be used[6]. The Biot number is defined as:

$$Bi = \frac{Lh}{k}, \tag{2.8}$$

where h is the coefficient of heat transfer, L is the characteristic length, and k is the thermal conductivity of the body.

The use of the lumped-capacitance model greatly simplifies description of conduction between sections of the motor and the cooling mechanism into a stack of flat plates and fins. The rate of heat transfer in conduction can be described by the following Fourier conduction equation,

$$\dot{Q} = -k_t A \frac{\Delta T}{L}, \tag{2.9}$$

where k is the thermal conductivity, A is cross-sectional surface area, and ΔT is the temperature difference across the length L. For a flat plate, heat transfer via

conduction can be expressed as an impedance $R_{cond} = \frac{L}{k_t A}$[6].

2.5 Previous Work

Deron Browne pursued a similar active-cooling project in 2016, in which he air-cooled the outer surfaces of a closed-housing inrunner Maxon motor to investigate improvements in torque density[2]. His methodology involved running the 48V BLDC motor with a steady 5A, 10W power input. The Maxon motor has a terminal resistance of 0.21Ω, so his heat generation in the windings was approximately 5.25W.

Browne's experiments found that despite causing a dramatic reduction of housing to ambient thermal resistance (keeping the temperature of the housing close to ambient temperature), forced convection at the outer surface of the motor was not able to significantly increase torque density. In a closed system like the inrunner Maxon motor, the winding stack only has a small total surface area contacting the housing since it is not press-fit during assembly; nearly all generated heat is transferred first by convection through air gap between the windings and the housing before leaving the motor. Increasing the effective surface area available for conductive cooling could potentially increase the effectiveness of his methods.

Chapter 3

Thermal Circuit Model

A thermal circuit model of the U8 permanent-magnet brushless motor was constructed to describe the rate of temperature change in the windings observed via experiment. Parameters in the model were a combination of datasheet entries (Appendix A) and calculated parameters chosen to fit the experimental data. This model was then used to predict thermal performance improvement under active cooling.

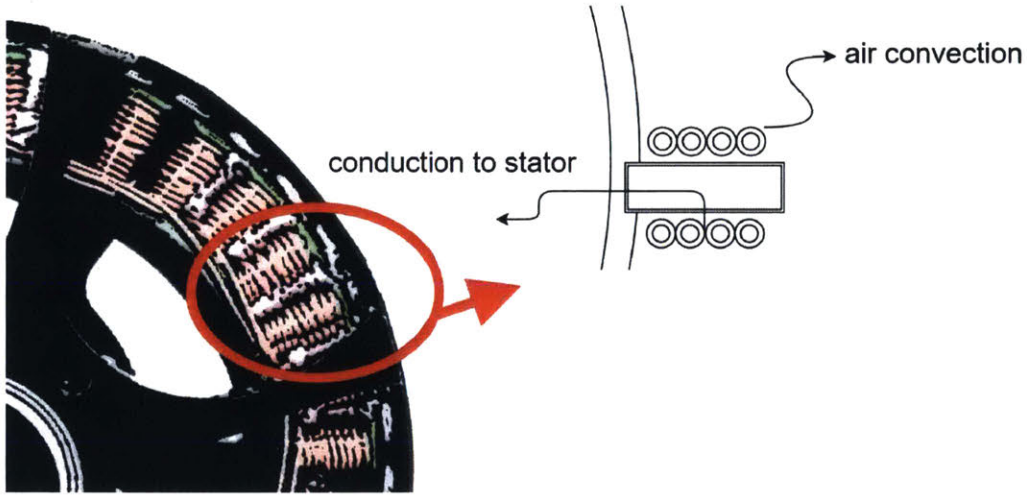

Figure 3-1: U8 motor and diagram of heat flow pathways from the windings to the motor housing.

3.1 Experimental

The U8 motor was rigidly coupled to a Futek TFF600 reaction torque sensor (Appendix A), which measured output torque from the motor and prevented it from spinning. Two K-type thermocouples attached to the windings and the aluminum motor housing monitored change in temperature as current was applied to the stalled motor. Additionally, voltage across the motor wires was measured in order to monitor changing terminal resistance.

During the test, power supply leads were attached to two of the motor wires and the third was left floating. The rotor angle was manually adjusted before the beginning of the test to maximize output torque; then the motor was locked against the shaft coupling with a set screw. The motor was allowed to return to room temperature before the test began.

A constant 11A current (104% rated max. continuous current) was supplied to the motor until winding temperature reached 55°C (a conservative temperature threshold to avoid harming the motor); then the power supply was shut off and the motor was allowed to cool down until the windings reached ambient temperature. Supply voltage was allowed to change during the course of the experiment.

3.1.1 Apparatus

- Power Supply
- Reaction Torque Sensor: TFF600 2000 in-lb, Futek. Irvine, CA, USA
- Torque Sensor Digital Display: IPM500, Futek. Irvine, CA, USA
- Thermocouple Amplifiers: MAX31855 breakout, Adafruit. NYC, USA
- Type-K Thermocouples ±5°C
- Arduino microcontroller (for thermocouples and timer)
- Voltmeter

3.1.2 Preliminary Observations

In the unaltered U8 motor with ambient temperature 21.5°C, winding temperatures reached 55°C within 120 seconds. The temperature of the motor housing also rose as heat dissipated from the windings, reaching a maximum temperature of 26.5°C approximately 100 seconds delayed from when the windings reached peak temperature.

Once the winding temperature exceeded 55°C, the power supply was turned off. Both heating and cooling curves appear to be first-order step responses. The time-constant for cooling the windings was observed to be approximately 160 seconds.

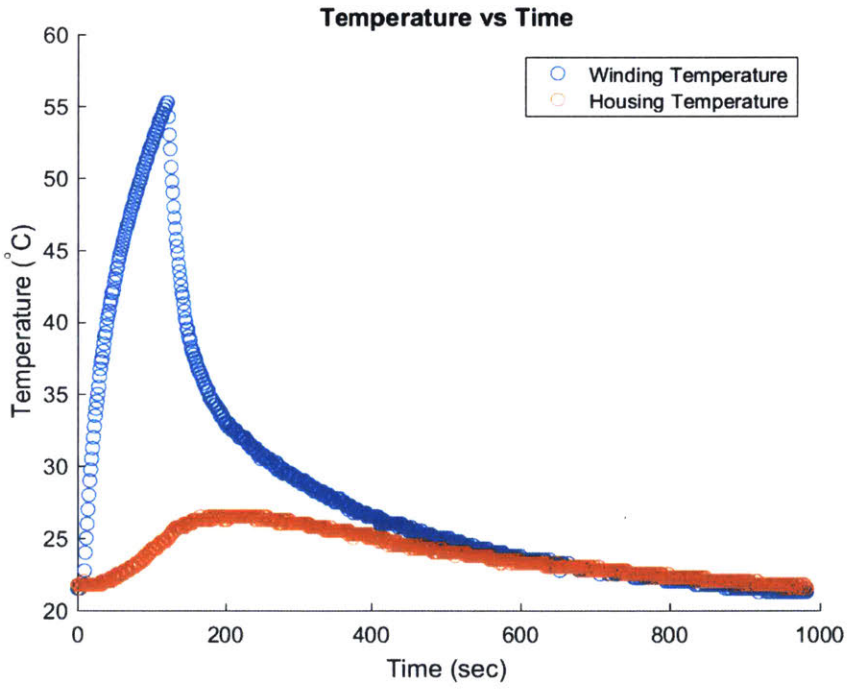

Figure 3-2: Experimental winding and housing temperatures vs time for constant 11A stall current.

3.2 Mathematical Modeling

3.2.1 Assumptions

As outlined in section 2.4, the thermal model for this thesis is simplified with a number of assumptions. First, all heat transfer between sections of the motor is assumed to

be via Fourier conduction and Newtonian convective cooling. Taken together, these mechanisms of heat transfer can be described by

$$\dot{Q} = k\Delta T, \tag{3.1}$$

where k is some constant to be determined experimentally. Therefore, temperature change in the windings due to heat flow is simplified to a single resistive parameter dependent only on temperature difference ΔT. Similarly, heat transfer from the casing to the surrounding environment is also modeled as a passive resistor. This assumption is validated by estimating the Biot number of the stator. Using the datasheet terminal resistance 186 mΩ and a winding diameter of 1mm, the length of the windings is estimated to be 8.7m and the effective surface area 273.18cm^2. L in the Biot number equation is considered the stator volume over surface area, h is the heat transfer coefficient for enamel insulation[9], and k is the conductivity of laminated steel. The Biot number of the stator was estimated to be 0.003, so the use of lumped parameter modeling is valid. In addition, thermocouple temperature measurements taken at the surfaces of the motor sections are assumed to be the true temperature values.

Second, heat transfer in the motor is assumed to be a first-order system involving only thermal capacitances and resistances. This assumption is validated by the data pictured in Figure 3-2, which closely follow the curvatures of RC charging and discharging circuits.

Third, although both specific heat and thermal resistance values for materials vary with temperature these parameters are assumed to be constant for the purposes of this thesis.

3.2.2 Thermal Circuit

The thermal model characterizing motor behavior is split into separate heating and cooling RC circuits, each with their own time constant and slope.

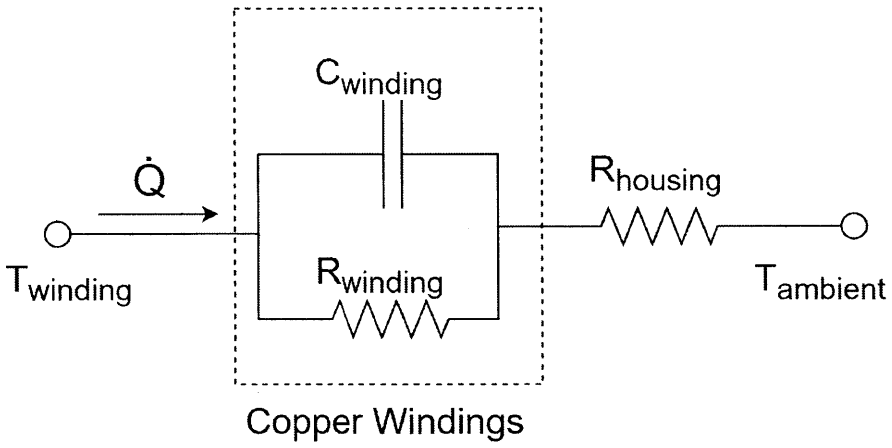

Figure 3-3: First-order thermal circuit model for constant-current heating. Heat generated in the windings via resistive heating is transferred to the rest of the motor, creating a difference in temperature.

Heating Circuit

Heat $\dot{Q}$ enters the system through resistive heating as electrical current is applied to the motor. Current is held constant, but winding resistance varies with temperature. The heat flow driving this system therefore takes the form $\dot{Q}(x) = ax + b$, where x is the winding temperature T_w. Combining equations 2.4 and 2.5 yields

$$\begin{aligned} a &= \alpha I^2 R_{electrical} \\ b &= I^2 R_{electrical}. \end{aligned} \tag{3.2}$$

As shown in Figure 3-3, the thermal circuit models heat flow through the windings as a parallel RC circuit and simplifies heat flow through the rest of the motor as a steady-state resistor. The model assumes that transient behavior of the windings dominates the system, therefore extraneous parallel capacitances are not considered.

The temperature of the windings T_w as a function of time is described by the following equation:

$$T_w(t) = T_a + \frac{b}{C(1-aR_h)^2}(1 - e^{\frac{-t}{\tau_{heating}}}), \quad \tau_{heating} = \frac{R_w C(1-aR_h)}{1-a(R_w+R_h)}. \tag{3.3}$$

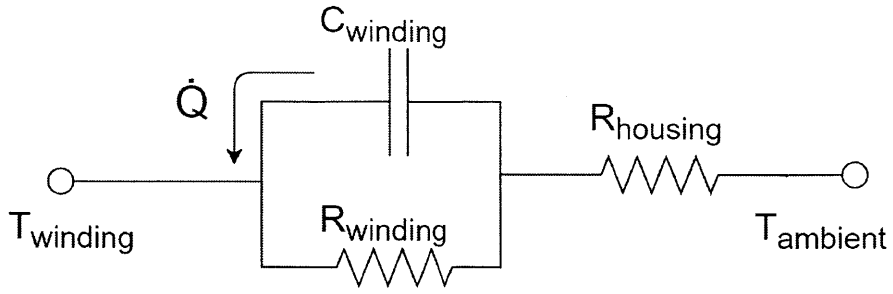

Figure 3-4: First-order thermal circuit model for cooling with no current source. Heat flow is driven by the temperature difference of the thermal capacitor.

Cooling Circuit

The capacitor in the cooling circuit model (Figure 3-4) begins at a temperature T_{init} and releases stored heat into the motor as it slowly returns to thermal equilibrium with its surroundings. This rate of heat release $\dot{Q}$ is solely dependent on the thermal capacitance and resistance of the windings.

The temperature of the windings as the motor cools down is modeled by

$$T_w(t) = (T_{init} - T_{amb})e^{\left(\frac{-t-t_{init}}{\tau_{cooling}}\right)}, \quad \tau_{cooling} = R_w C. \tag{3.4}$$

Fitting Parameters

The thermal capacitance of enamel-insulated copper wire was estimated from the copper volume and the isobaric specific heat capacity. Winding thermal resistance was then calculated from the cooling time constant $\tau_{cooling} = R_w C$. R_h was finally chosen to best fit the data. Table 3.1 lists numerical values for these parameters.

This simulation closely follows the heating curve of the motor; however, its exponential cooling curve fails to capture the initial transient slope seen in the experimental data. This discrepancy could be attributed to the absence of radiative cooling in this

Table 3.1: Circuit Model Parameters, Unaltered Motor

I (A)	R_w (K/W)	C (J/K)	R_h (K/W)	a (W)	b (W)
11	1.2	133.3	12.14	0.0878	22.506

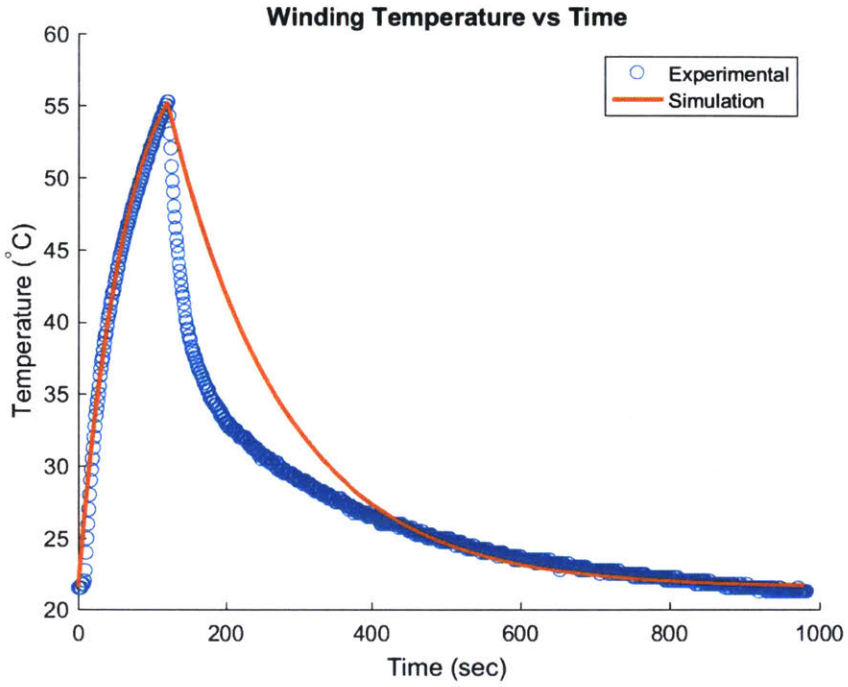

Figure 3-5: Observed and simulated winding temperatures vs time, unaltered U8.

model, or to the ignored temperature dependance of the winding thermal capacitance and resistance. The model does exhibit the same settling temperatures and time constants for both heating and cooling conditions, and therefore can be considered accurate for cooling periods larger than one time constant (160 sec).

3.2.3 Performance Predictions

The addition of a heat sink has a number of effects on the thermal circuit. The added physical mass increases the thermal capacity of the system by some fixed amount, and the increased forced conduction/convection affects R_h. However, adding a heat sink is not expected to affect the thermal resistance R_w of the windings themselves. Figure 3-6 shows the predicted effects of varying C and R_h.

Contrary to expected circuit theory, the R_h parameter in the model seems to be inversely related to actual housing thermal resistance. This phenomenon is likely due to modeling R_h as a single resistor in series with the winding parameters, which has the effect of floating the "voltage" of the thermal capacitance. However, the

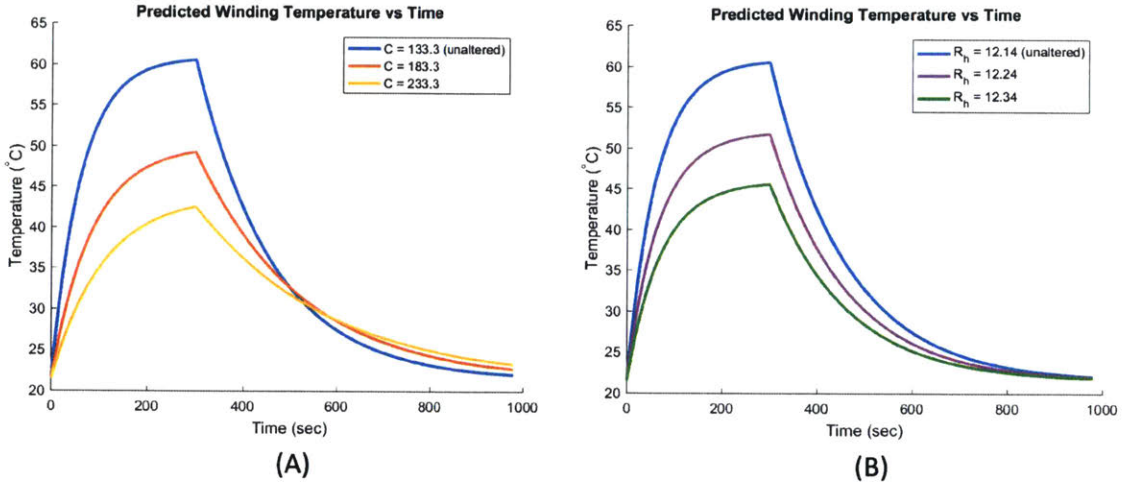

Figure 3-6: Predicted winding temperatures vs time. (A) shows effect of varying C and (B) shows effect of varying R_h.

inverse relationship between R_h and housing thermal resistance is consistent with the expectation that a lower thermal resistance in the housing will increase heat flow (modeled as circuit current) out of the system.

Chapter 4

Active Cooling Heat Exchanger

A heat exchanger prototype was fabricated to validate the predictions based on the circuit model developed in the previous chapter. Experiments were first run with the motor-heat exchanger system passively cooled in still-air in order to determine new circuit parameters. Experiments were repeated with the system using fan-based active cooling, then the results of these experiments were compared against the thermal performance of the unmodified U8 motor. In addition, simulations based on this model were used to predict performance at varying input currents.

4.1 Passive Heat Exchanger

The heat exchanger consists of a commercial CPU heat sink attached to the U8 motor with four copper heat pipes. These heat pipes were held in contact against the stator laminatations with an aluminum insert, machined to press-fit inside the interior cavity of the stator. The insert serves both to hold the heat pipes in a known position and to improve heat conduction of the housing.

The heat pipes in this system (Appendix A) have sintered-powder wicks and use de-ionized water as their working fluid. The heat conduction of sintered heat pipes is considered independent of both orientation and gravity.

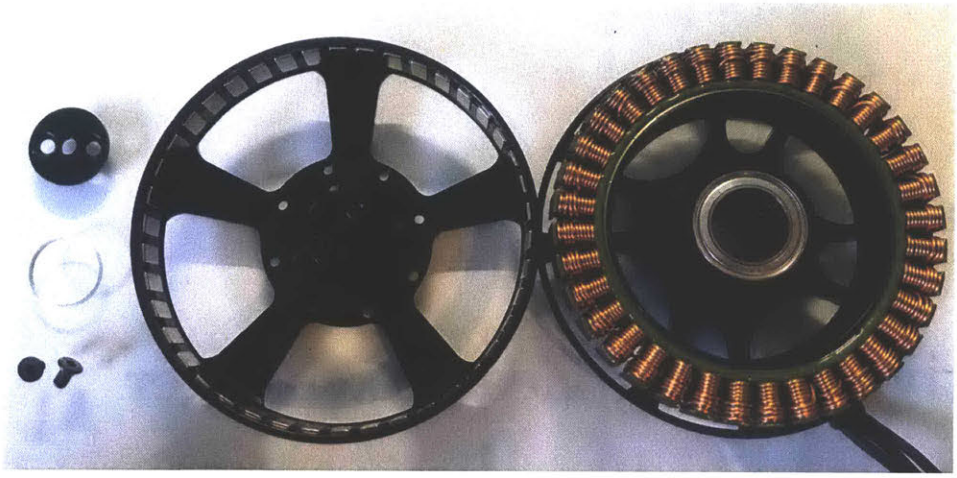

Figure 4-1: Image of disassembled U8 motor. An aluminum insert was machined to match the interior cavity of the stator (right). This insert positioned four heat pipes in close proximity to the windings and ensured contact to facilitate conduction.

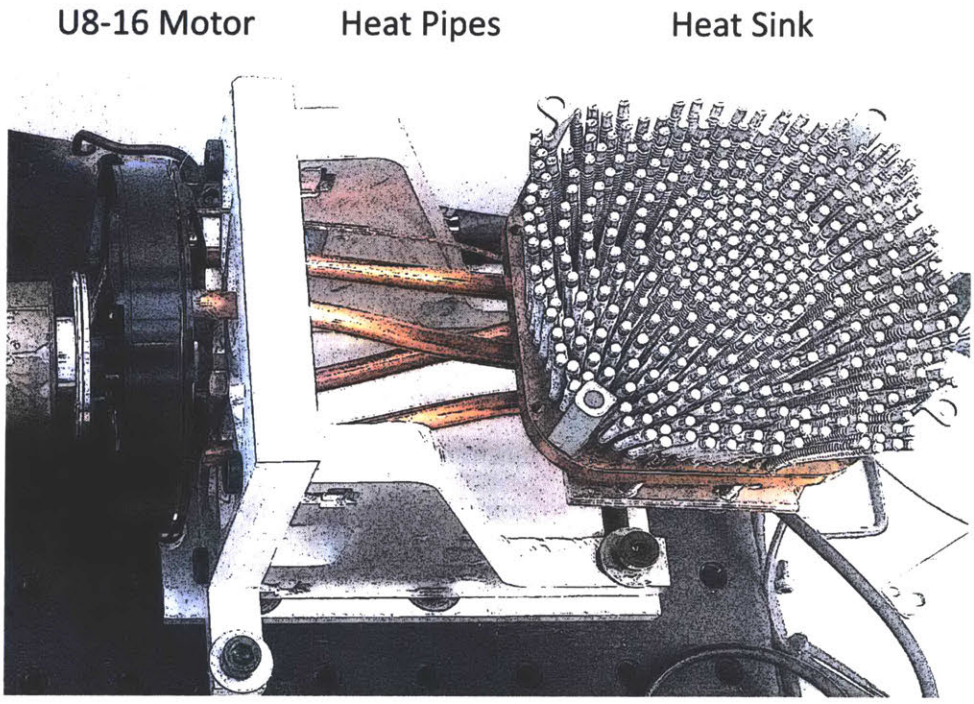

Figure 4-2: Image of passive cooling system comprised of heatpipes clamped underneath a copper-aluminum heat sink. The pipes are seated in an aluminum insert such that they are located 1mm from the stator laminations and 2mm from the windings.

4.1.1 System Characterization

Winding temperature increase for a constant 11A current input was monitored in an identical experiment to the one described in Section 3.1, then model parameters were chosen to fit the data.

Figure 4-3: Image of experimental setup. Components from left to right: torque readout, voltage readout, torque sensor coupled to motor shaft, motor containing heatpipe insert, heat exchanger.

As predicted by Section 3.2.3, the addition of this heat exchanger system changed the thermal circuit values of C and R_h and left the winding thermal resistance R_w unchanged. The updated values of the circuit parameters are shown in Table 4.1, and the resulting simulated temperature curve is shown in Figure 4-4.

Table 4.1: Circuit Model Parameters, Passive Cooling

I (A)	R_w (K/W)	C (J/K)	R_h (K/W)	a (W)	b (W)
11	1.2	240	11.96	0.0878	22.506

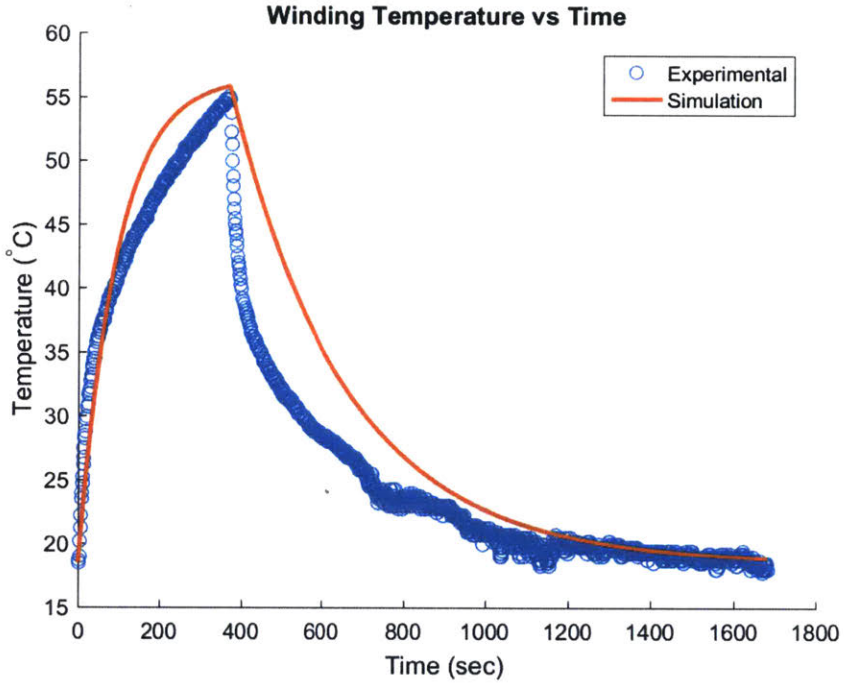

Figure 4-4: Observed and simulated winding temperatures vs time, passive cooling

4.1.2 Non-linearities of R_h

When taking experimental data, R_h was discovered to have a dependence on input current, described by the following equation:

$$R_h = \frac{R_0}{I^2}, \tag{4.1}$$

where R_0 was experimentally determined to be 1447. It remains unclear what physical phenomenon would give R_h additional dependencies on heat generation $I^2 R_{electrical}$ that were not already addressed by the parameters a and b from Equation 3.2, but defining R_h to be dependent on I^{-2} does make the model more accurate for a range of input currents (Figure 4-5).

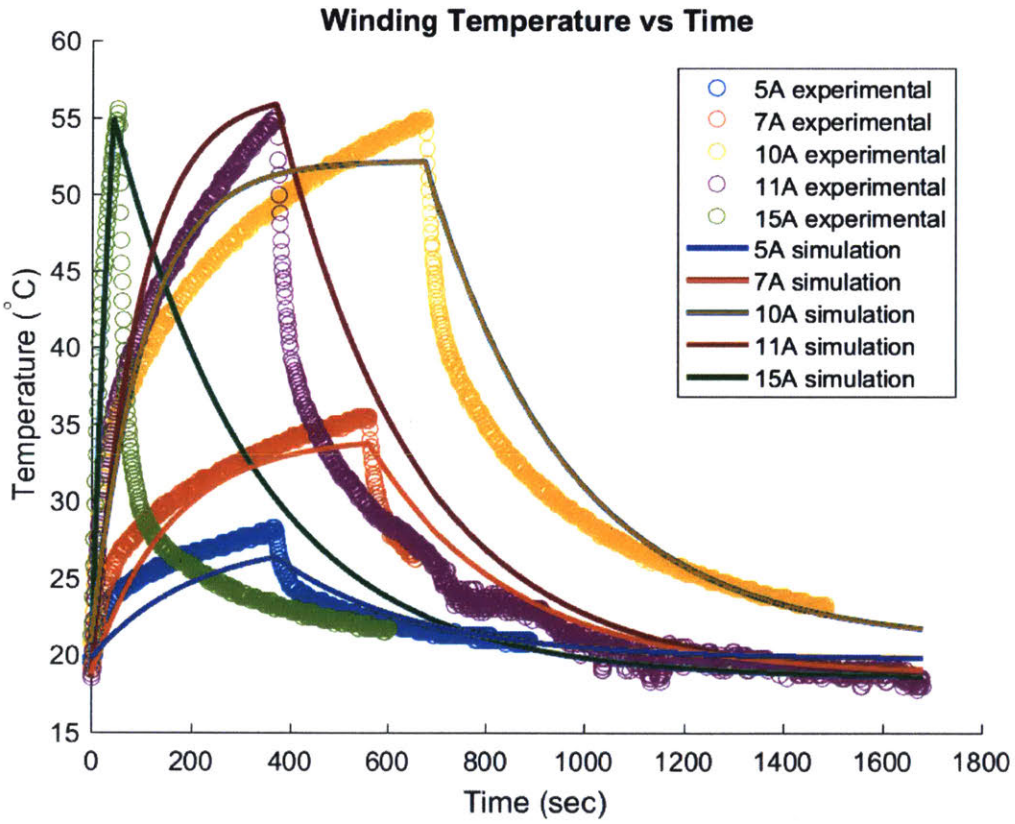

Figure 4-5: Observed and simulated winding temperatures vs time for different input currents, passive cooling

4.2 Fan-assisted Heat Exchanger

A commercial desktop oscillating fan (Holmes HAOF87BLZ-UC) was used to increase air flow through the heat sink. The 84-W oscillating fan was kept powered on for both heating and cooling procedures. Again, temperatures were monitored under 11A current to determine model parameters.

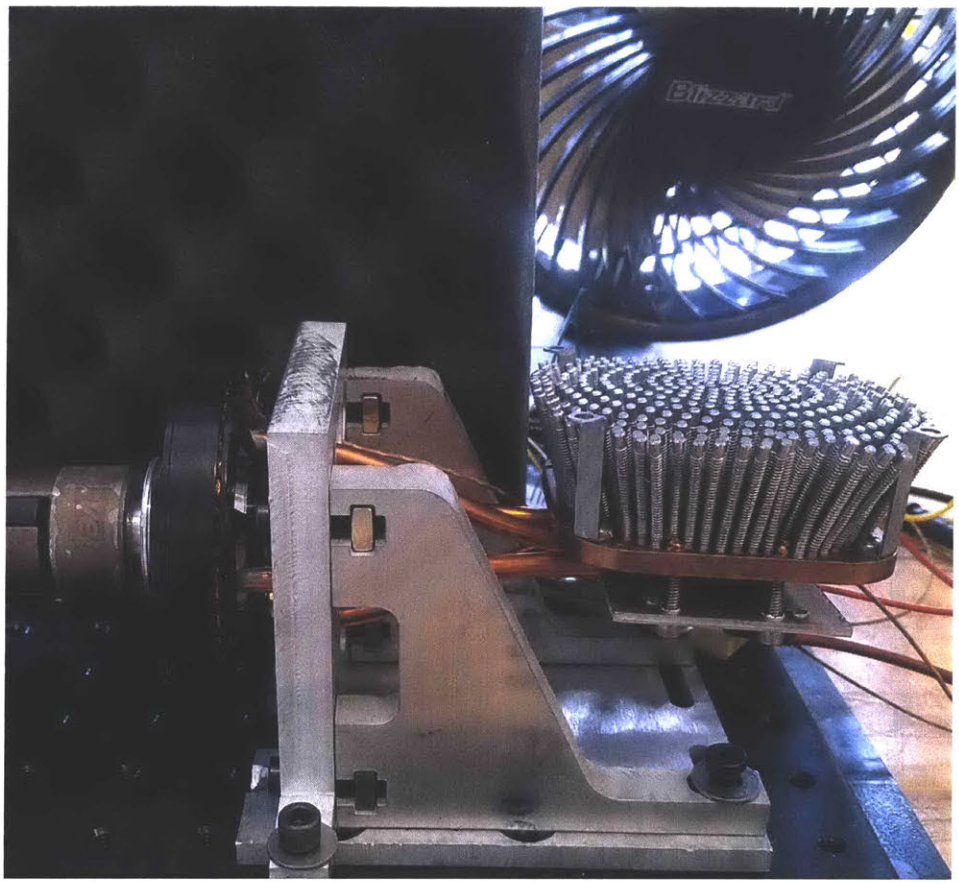

Figure 4-6: Experimental setup with fan cooling. A foam wall minimizes air flow directly over the windings, such that increased air flow only affects the heat sink.

The active cooling model has a larger C value but identical R_h as the passive circuit.

Table 4.2: Circuit Model Parameters, Fan Cooling

I (A)	R_w (K/W)	C (J/K)	R_h (K/W)	a (W)	b (W)
11	1.2	250	11.96	0.0878	22.506

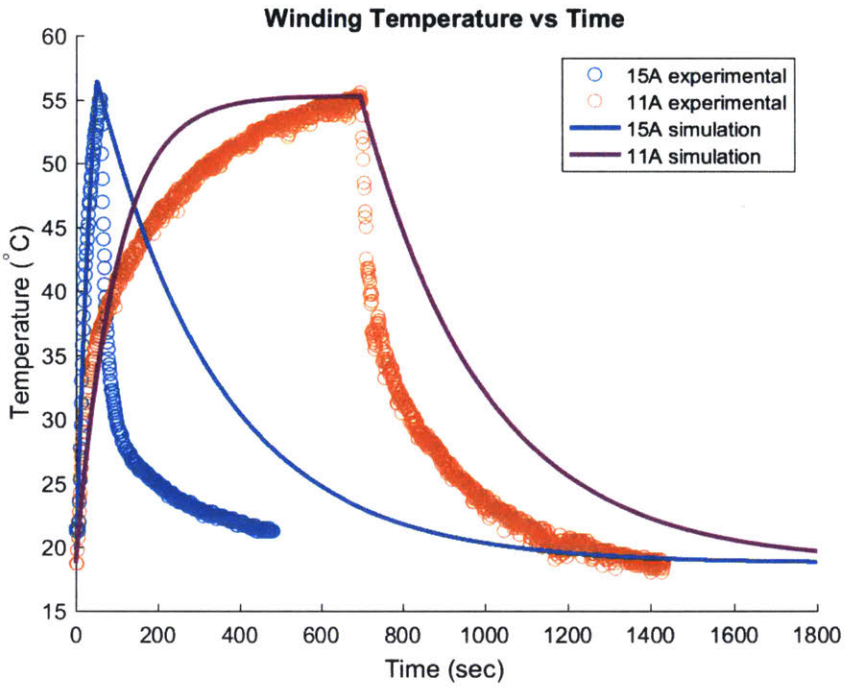

Figure 4-7: Observed and simulated winding temperatures vs time for different input currents, active cooling. For 15A input current, winding temperature reached 55°C in 56s.

Similar to the passive model, the active-cooling circuit model does not accurately capture the curvature when cooling with a time constant defined as $R_w C$. There is a high likelihood that when there is no resistive heating additional nonlinear heat transfer pathways do have an effect on heat transfer, which makes the circuit model overly complex for the scope of this project. However, the model does reasonably match the heating part of the experimental data in terms of time required to reach a threshold "dangerous temperature". This thesis will therefore consider the simulated temperature curves to be accurate in heating and a conservative estimate in cooling.

4.3 Thermal Effectiveness

Projecting the experimental heating data for the unaltered U8 and motor-heat exchanger systems allows for several notable observations. For a given input current of 11A, the addition of this heat exchanger prototype even in still-air increases the time

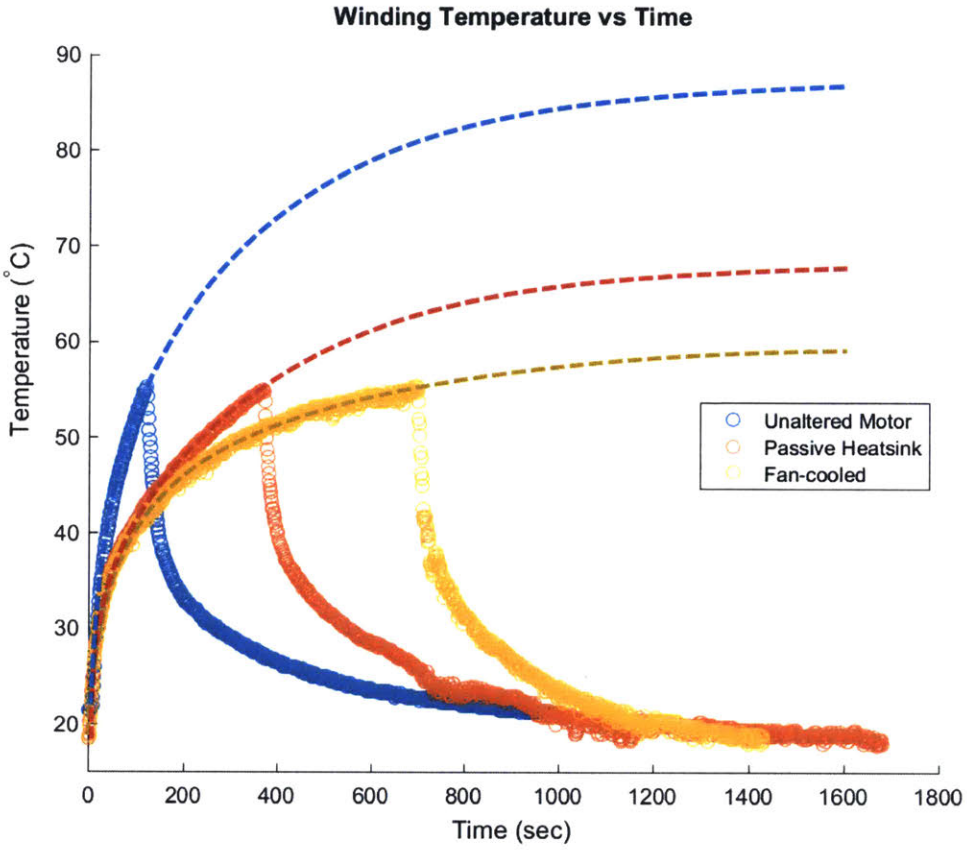

Figure 4-8: Comparison of observed winding temperatures vs time for unaltered, passive, and fan-cooled motor, 11A. Dotted lines extend exponential heating curves to projected steady-state temperatures.

constant by approximately 20 seconds and lowers the steady-state temperature by approximately 25°C. With a fan blowing, the steady-state temperature of the motor remains below 60°C. However, running this motor at 11A generates barely over 1Nm of torque (104% of max. continuous torque).

Adding a heatsink allows the U8 to be run with 15A input current (142% max. continuous current) for up to 50 seconds before winding temperatures exceed 55°C. With a fan blowing, this operating time is extended to a maximum of 56 seconds.

The U8-16 motor can supply a maximum stall torque of 3.2Nm if supplied with 35A current (330% max. continuous torque). But even with the heat exchanger prototype, sustaining 35A current is not feasible. Both passive and active cooling

simulations exceeded 105°C after 4 seconds. The conservative estimate for cooling time constant is 288 seconds for passive cooling, and 300 seconds for active cooling.

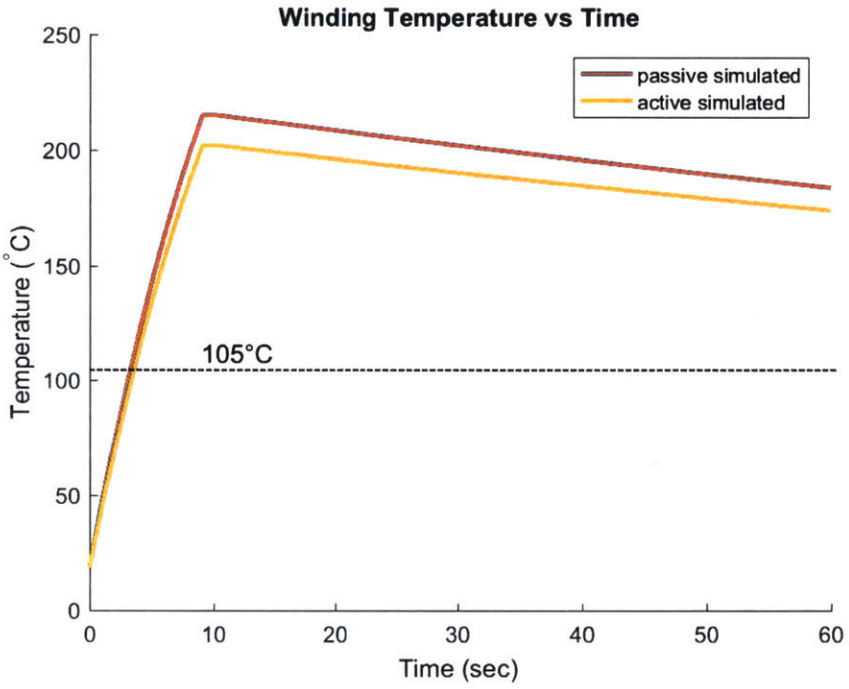

Figure 4-9: Simulation of winding temperatures vs time for passive and fan-cooled motor at stall current, 35A. The dotted black line at 105°C identifies point of thermal failure for the winding enamel.

In prosthetic applications, the actuator would only need to receive large amounts of current intermittently and for a short duration of time. Figure 4-10 simulates winding temperature rise when the motor is supplied stall current for 1 second. Under these conditions, the winding temperature reaches a manageable 47°C and 45.5°C for the passive and active motor, respectively, but requires 25 minutes to fully return to ambient temperature.

For such high currents, simulated air cooling with a desktop fan achieves very little. Hypothetical heating curves for systems with thermal capacitances of 300 J/K and 400 J/K were also plotted. Such hypothetical systems also experienced rapid heating and long cool-down times, though the overall temperature increase was less severe.

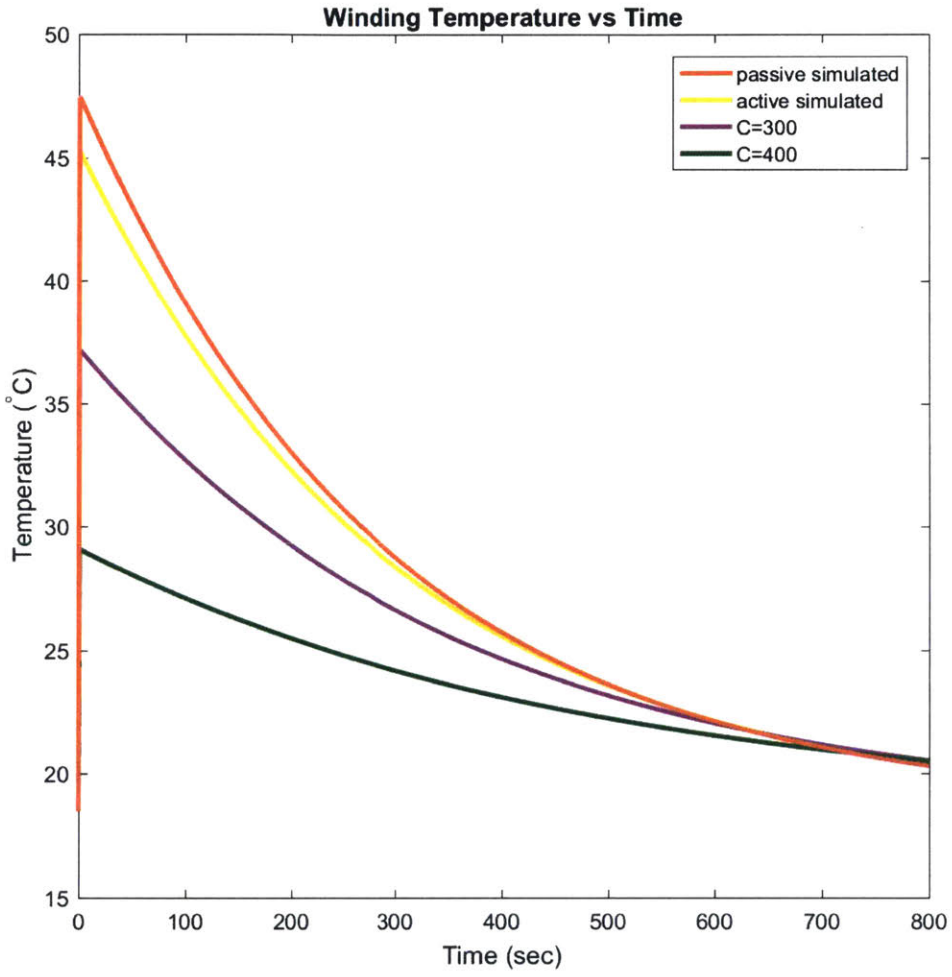

Figure 4-10: Simulation of winding temperatures vs time for passive(C=240), fan-cooled motor(C=250), and hypothetical thermal capacitance systems when supplied 35A stall current for 1 second.

Chapter 5

Tradeoffs of Active Cooling vs Increasing Motor Size

The previous chapters discussed the potential for active cooling mechanisms to slow the rate of temperature rise based on the results of a fan-based heat sink prototype. For input currents around the rated maximum continous torque, the addition of a heat exchanger improves the heating time constant by 100%. By actively cooling the heat sink, this time constant is improved by 360% compared to the unaltered motor. For input currents significantly exceeding the rated continuous operating current, the use of fan-based cooling in this prototype made less of a difference than the presence of the heat exchanger itself.

The prototype motor-heat exchanger system weighed 867g and had an estimated package size of 7.0"x 3.5"x 2.5". Compared to the unaltered motor, this prototype increased weight by 360% and package volume by 475%.

The prototype built for this project did not try to be mass or volume efficient; the design choices instead focused on maximizing simplicity of fabrication and ease of running experiments. However, a more efficient heat-pipe system will increase the thickness of the motor by at least the diameter of the heatpipe (6mm for this project).

Assuming a more size and weight efficient heat exhanger exhibits similar thermal performance to this prototype, a case could still be made that a larger motor would provide overall torque improvement. A similar motor to the U8 used in this project

is the RCTiger U10 (Appendix A), an open frame brushless 100KV motor with identical torque constant of 0.1Nm/A. Its maximum continuous operating current is 35A, equivalent to the U8's current at stall. At max. operating current, the U10 can run for 180 seconds before exhibiting thermal failure (where "thermal failure" is not well-defined by the manufacturer).

Replacing the motor in this project with the larger U10 motor results in similar torque improvement with a smaller increase in weight and package volume (167% and 130%, respectively) than the original prototype, and would likely be smaller and lighter than even a more efficient cooling system.

Conversely, if heat pipes connected the motor stator to the preexisting structure of the prosthesis housing the use of this housing as a passive heat sink is likely to improve torque performance. For a hypothetical prosthesis housing with similar thermal capacitance and resistance to ambient as the heatsink used in this project, a U8 motor could be used for applications that would require a U10 if abiding by manufacturer specifications.

Chapter 6

Summary and Conclusion

This thesis investigates the effectiveness of improving heat transfer away from the windings to improve motor torque performance. Simulations that described winding temperature as a function of input current were validated by experiments on a physical prototype. Results from the motor-heat exchanger system support thermal model predictions that improving thermal capacitance and reducing thermal resistance through the housing will allow motors to be safely run with input current levels above their thermal saturation limit, although the increase in torque performance is accompanied by an increase in weight and package volume.

Active cooling enables motors to be run at their full torque capacity for short periods of time, which holds promise for prosthetic applications. It is hoped that the effort put into characterizing the effects of cooling on torque production will help optimize future actuator designs.

6.1 Improvements and Future Work

Further work is necessary to refine the predictions made in this thesis. The thermal circuit model developed is a linearized simplification of heat transfer through the motor; therefore, its parameters do not have directly correspond to material properties such as specific heat capacity or material thermal resistance. A more complex and accurate model would need to be constructed in order to fully predict thermal behavior

without relying on experimental observation. Such a model might then be able to explain the additional dependence on current needed to make values of R_h fit observed behavior, which currently does not have an analogue to physics. A circuit with thermal winding capacitance and resistance values tied to material parameters would additionally be able to better follow the temperature curves for cooling, which this circuit model does not do well.

A future cooling system could consider the effects of more powerful and space-efficient methods of active cooling that directly contact the winding enamel to see if the rate of heating is improved for stall current. Currently, the thermal resistance of the enamel insulation is the main limitation on the effectiveness of cooling methods.

Appendix A

Specifications & Datasheets

A.1 RCTiger U8-16 100KV

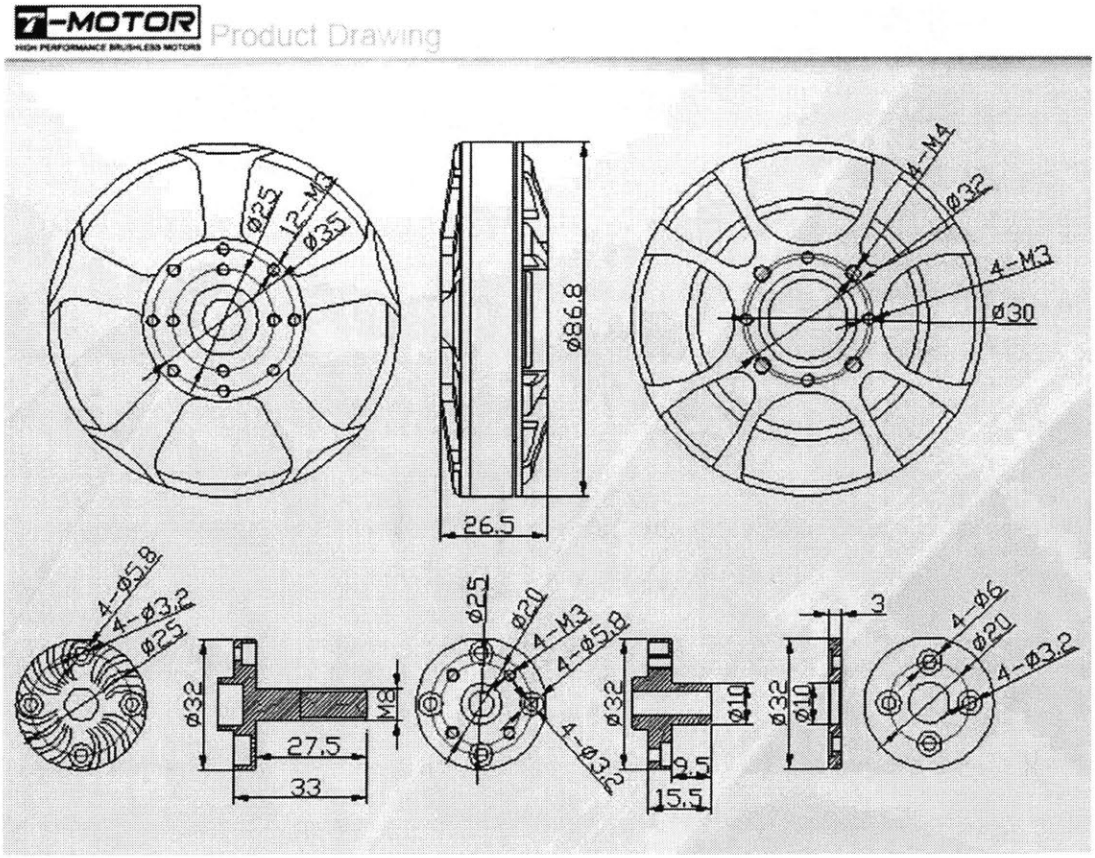

Table A.1: U8-16 100KV parameters

Cont. Max Torque	1.01 Nm
Stall Torque	3.2 Nm
Stall Current	35 A
No-load Speed	2200 rpm
Input Voltage	6S
Rotor Inertia	0.000565 kg-m^2
Winding Resistance	186 mΩ
Winding Inductance	0.136 mH
Weight	240 g

Item No.	Volts (V)	Prop	Throttle	Amps (A)	Watts (W)	Thrust (G)	RPM	Efficiency (G/W)	Operating temperature(℃)
U8 KV100	22.2 (6S)	T-MOTOR 26*8.5CF	50%	1.6	35.52	710	1200	19.99	38
			65%	2.7	59.94	1110	1460	18.52	
			75%	3.8	84.36	1400	1650	16.60	
			85%	5.1	113.22	1790	1820	15.81	
			100%	5.9	130.98	1980	1920	15.12	
		T-MOTOR 27*8.8CF	50%	1.7	37.74	770	1160	20.40	38
			65%	3	66.6	1200	1430	18.02	
			75%	4	88.8	1530	1620	17.23	
			85%	5.4	119.88	1880	1790	15.68	
			100%	6.4	142.08	2140	1890	15.06	
		T-MOTOR 28*9.2CF	50%	1.8	39.96	860	1130	21.52	40
			65%	3.3	73.26	1300	1400	17.75	
			75%	4.6	102.12	1660	1580	16.26	
			85%	6.2	137.64	2100	1730	15.26	
			100%	7.2	159.84	2350	1850	14.70	
		T-MOTOR 29*9.5CF	50%	2	44.4	930	1100	20.95	41
			65%	3.8	84.36	1530	1380	18.14	
			75%	5.2	115.44	1870	1550	16.20	
			85%	7.1	157.62	2320	1700	14.72	
			100%	8.1	179.82	2580	1820	14.35	
	44.4 (12S)	18x6 wood prop	50%	1.4	62.16	780	2580	12.55	42
			65%	2	88.8	1070	3000	12.05	
			75%	2.5	111	1280	3350	11.53	
			85%	3.5	155.4	1630	3720	10.49	
			100%	4.6	204.24	2020	4120	9.89	
		20x6 wood prop	50%	1.5	66.6	820	2420	12.31	43
			65%	2.4	106.56	1230	2930	11.54	
			75%	3.2	142.08	1550	3260	10.91	
			85%	4.3	190.92	1920	3750	10.06	
			100%	5.8	257.52	2430	4070	9.44	
		22x6 wood prop	50%	1.9	84.36	1100	2350	13.04	45
			65%	3.4	150.96	1720	2850	11.39	
			75%	4.4	195.36	2130	3200	10.90	
			85%	6	266.4	2660	3530	9.98	
			100%	8.1	359.64	3330	3900	9.26	

Notes:The test condition of temperature is motor surface temperature in 100% throttle while the motor run 10 min.

A.2 RCTiger U10 100KV

T-MOTOR

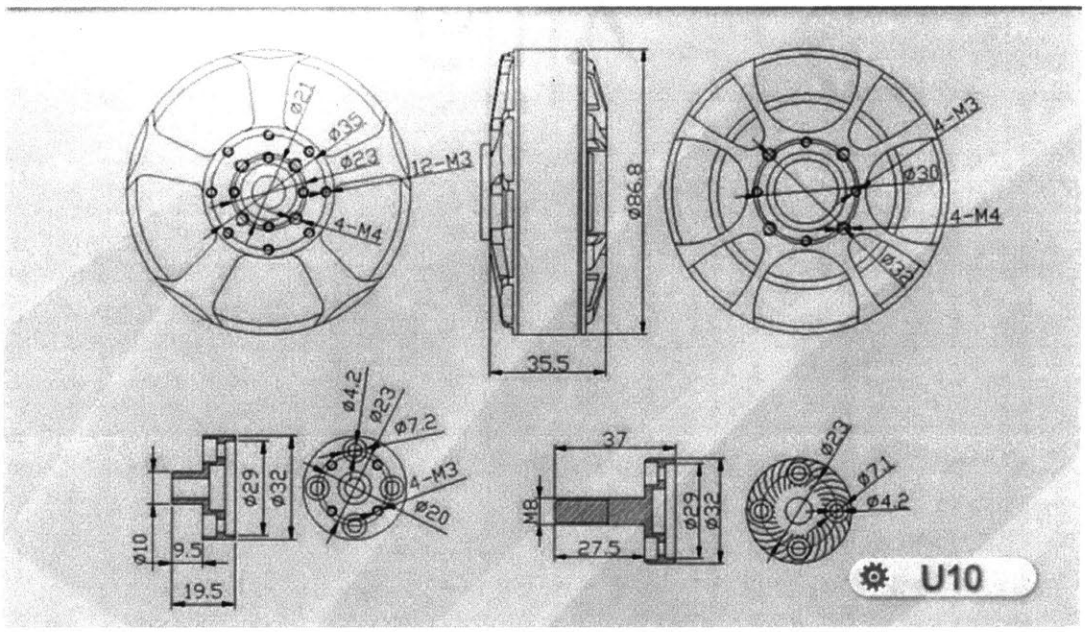

Specifications:

KV.....100

Configu ration.....36N42P

Shaft Diameter.....15mm

Motor Dimensions (Dia.*Len).....Φ86.8×35.5mm

Weight(g).....400g

Idle current(10)@10v(A).....1.4A

No.of Cells(Lipo).....6-12S

Max Continuous current(A)180S.....35A

Max Continuous Power(W)180S.....1500W

Max. efficiency current.....(3-20A)>89%

Internal resistance.....95mΩ

A.3 Futek TFF600

FUTEK
ADVANCED SENSOR TECHNOLOGY, INC.

MODEL TFF600
Reaction Torque Sensor with Thru Hole Center

FEATURES

- Easily integrates into OEM applications
- Designed for Torque auditing
- Aluminum & stainless-steel construction
- Strain gauge based

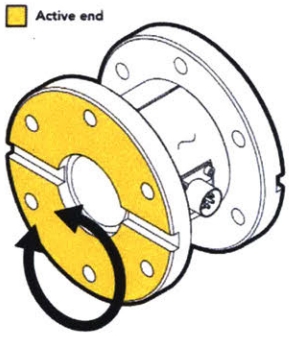

– Output (CCW)
+ Output (CW)

SPECIFICATIONS	
PERFORMANCE	
Nonlinearity	±0.2% of RO
Hysteresis	±0.2% of RO
Nonrepeatability	±0.2% of RO
ELECTRICAL	
Rated Output (RO)	2 mV/V nom
Excitation (VDC or VAC)	18 max
Bridge Resistance	350 Ohm nom
Connection	6 Pin BENDIX Receptacle (PT02E-10-6P)
Connector Code	CC1
MECHANICAL	
Weight (approximate)	See chart on next page
Safe Overload	150% of RO
Material	Aluminum (Cover) Aluminum (Flexure 2000 in-lb) 17-4 PH stainless steel (Flexure 10000 in-lb)
IP Rating	IP40
TEMPERATURE	
Operating Temperature	–60 to 200°F (–50 to 93°C)
Compensated Temperature	60 to 160°F (15 to 72°C)
Temperature Shift Zero	±0.002% of RO/°F (0.0036% of RO/°C)
Temperature Shift Span	±0.002% of Load/°F (0.0036% of Load/°C)
CALIBRATION	
Calibration Test Excitation	10 VDC
Calibration (standard)	5-pt CW
Calibration (available)	5-pt CW & CCW
Shunt Calibration Value	60.4 kOhm

Sensor Solution Source
Load · Torque · Pressure · Multi-Axis · Calibration · Instruments · Software

www.futek.com

ANS Z540-1 · ISO 17025 · ISO 9001 · ISO 13485 · U.S. Manufacturer

Item #	in-lb	Nm	Natural Frequency (Hz)	Torsional Stiffness (ft-lb/rad)	Weight (kg)
FSH00681	2000	225	1600	45300	0.9

A.4 CCI Sintered Heat Pipes

Part Number	Structure	Length	Original Diameter	Thickness	Thermal resistance of pipe Rpipe in (K / W)	Operating Max Power (W)
00C93390101	Sintered	100	5	5	0.02 – 0.04	40
00C93400101	Sintered	150	6	6	0.02 – 0.03	65
00C93410101	SM	150	4	2	0.65 – 0.90	15
00C93420101	SM	200	6	2	0.35 – 0.60	30
00C93430101	Groove	100	5	2.5	0.03 – 0.06	30
00C93440101	Groove	150	6	6	0.02 – 0.03	65
00C93450101	Groove	150	8	2.5	0.003 – 0.05	15
00C93460101	G+S	200	6	3.0	0.003 – 0.008	40
00C93470101	G+S	150	8	4.5	0.003 – 0.015	70
00C93480101	G+S	300	8	8	0.002 – 0.007	65

Bibliography

[1] S. K. Au, M. Berniker, and H. Herr. Powered ankle-foot prosthesis to assist level-ground and stair-descent gaits. *Neural Networks*, 21:654–666, 2008.

[2] D. A. Browne. Investigating the trade-offs involved in augmenting a dc brushless motor with and active heat sink in order to improve performance. Undergraduate thesis, Massachusetts Institute of Technology, 2016.

[3] D.H. Gates, J. Lelas, U. Della Croce, H. Herr, and P. Bonato. Characterization of ankle function during stair ambulation. In *2014 IEEE EMBS*, pages 4248–4251, Sept 2004.

[4] C. D. Hoover, G. D. Fulk, and K. B. Fite. Stair ascent with a powered transfemoral prosthesis under direct myoelectric contro. *IEEE/ASME Transactions on Mechatronics*, 18(3):1191–1200, June 2013.

[5] H. Crowell III, A. Boynton, and M. Mungiole. Exoskeleton power and torque requirements based on human biomechanics. Technical report, Army Res. Lab., Aberdeen Proving Ground, MD, Tech. Rep. ARL-TR-2764, Nov 2002.

[6] J. H. Lienhard IV and J. H. Lienhard V. *A Heat Transfer Textbook, 3rd Ed.* Cambridge, MA, 2000.

[7] G. Kenneally, A. De, and D. E. Koditschek. Design principles for a family of direct-drive legged robots. *IEEE Robotics and Automation Letters*, 1(2):900–907, 2016.

[8] D. Montone. Temperature effects on motor performance. Technical report, Pittman Motors, 2017.

[9] P. Mynarek and M. Kowol. Thermal analysis of a pmsm using fea and lumped parameter modeling. *Czasopismo Techniczne*, 1-E(8):97–107, 2015.

[10] M. L. Palmer. Sagittal plane characterization of normal human ankle function across a range of walking gait speeds. Master's thesis, Massachusetts Institute of Technology, Mechanical Engineering Department, June 2002.

[11] E. J. Rouse, L. M. Mooney, and H. M. Herr. Clutchable series-elastic actuator: Implications for prosthetic knee design. *International Journal of Robotics Research*, 33(13):1611–1625, 2014.

[12] S. Seok, A. Wang, D. Otten, and S. Kim. Actuator design for high force proprioceptive control in fast legged locomotion. In *2012 IEEE/RSJ International Conference on Intelligent Robots and Systems*, pages 1970–1975, Oct 2012.

[13] T. Spägele, A. Kistner, and A. Gollhofer. Modelling, simulation and optimisation of a human vertical jump. *Journal of Biomechanics*, 32:521–530, 1999.

[14] T-Motor. U8 motor, 2013.